Topics in Catalysis
https://doi.org/10.1007/s11244-026-02293-2

ORIGINAL PAPER

Energy Production from Cheese Whey Using Boron-Incorporated Graphene Oxide Catalyst in Plant Based Microbial Fuel Cells

Niyazi Alper Tapan[1] · Beyza Uysal[1] · Nurce Bilgili[1] · Pinar Cebeci[1] · Busra Akbulut[1] · Silver Gunes[1,2]

Accepted: 29 March 2026
© The Author(s) 2026

Abstract

Plant microbial fuel cells (PMFCs) represent a promising technology for sustainable bioelectricity generation while enabling organic waste valorization. In this study, boron-modified graphene oxide (BGO) electrocatalysts were synthesized via electrochemical exfoliation of 8B pencil graphite, followed by ultrasonication-assisted boron incorporation at 5 °C and 55 °C. ICP-OES analysis confirmed boron contents of 200.7 ppm and 651.7 ppm for BGO-5 and BGO-55, respectively. Raman spectroscopy revealed an increased I_D/I_G ratio for BGO-55 (0.82) compared to GO (0.68), indicating enhanced structural disorder and defect density, which is hypothesized to be associated with boron-induced perturbations within the graphene oxide framework. Electrochemical characterization (CV and EIS) demonstrated improved oxygen reduction (ORR) activity and reduced charge-transfer resistance for BGO-55, supporting the role of defect-enriched, boron-modified structures in facilitating electron transfer. When integrated into soil-based single sugar beet PMFC systems, BGO-55 significantly enhanced power density in both anode (0.936 mW m^{-2}) and cathode-modified (0.967 mW m^{-2}) configurations following whey supplementation. The improved performance is attributed to the synergistic interaction between increased boron content, defect-mediated electronic modulation, and enhanced ORR kinetics under substrate-enriched conditions. These findings suggest that low-temperature sonochemical boron incorporation offers a scalable and energy-efficient strategy to improve PMFC performance while promoting sustainable energy generation and agro-industrial waste utilization.

Keywords Plant microbial fuel cell · Boron · Graphene · Whey · Bioelectrochemical · Waste water treatment

1 Introduction

Solar, wind, geothermal, and hydrothermal energy are rapidly growing renewable sources, offering promising alternatives to non-renewable energy. However, their limitations, such as site dependency, high initial costs, and ecological impacts, remain making it difficult to expand their use on a larger scale. At this point, plant microbial fuel present as a noteworthy green energy alternative [1]. Nowadays, PMFC have attracted great interest in recent years due to their potential to generate clean, sustainable and environmentally friendly energy [2]. In addition, they can be used for wastewater treatment, and applications in systems like monitoring devices, sensors, and IoT devices [3]. Despite its promise, the PMFC technology requires further improvements to achieve better energy and economic viability [4].

Plant-based microbial fuel cells are bioelectrochemical systems capable of generating electricity through the oxidation of organic matter by microorganisms [2]. Photosynthetically produced organic compounds are released

✉ Niyazi Alper Tapan
atapan@gazi.edu.tr

Beyza Uysal
uyslbyzz@gmail.com

Nurce Bilgili
nurcebilgili@gmail.com

Pinar Cebeci
pcebeci14@gmail.com

Busra Akbulut
busrakbulut1@icloud.com

Silver Gunes
silver@gazi.edu.tr

[1] Chemical Engineering Department, Gazi University, Maltepe, 06570 Ankara, Turkey

[2] Faculty of Pharmacy, Gazi University, Etiler, 06330 Ankara, Turkey

Published online: 13 May 2026

from plant roots into the rhizosphere as root exudates. These biodegradable substrates are metabolized by electrogenic microorganisms colonizing the anode region. During microbial oxidation, electrons are transferred from the microorganisms to the anode surface via extracellular electron transfer mechanisms and subsequently flow through the external circuit to the cathode, where the oxygen reduction reaction occurs, thereby enabling electricity generation in PMFC systems.

Anodic and cathodic half-cell reactions in PMFC can be seen in Eqs. (1) and (2) where protons generated during oxidation of glucose substrate at the anode electrode are used for oxygen reduction at the cathode electrode [5].

$$C_6H_{12}O_6 + 6H_2O \rightarrow 6CO_2 + 24H^+ + 24e^-, E^0 = 0.014V \quad (1)$$

$$6O_2 + 24H^+ + 24e^- \rightarrow 12H_2O\,,\ E^0 = 1.23V \quad (2)$$

The electrical output of PMFC systems is governed by several coupled processes, including substrate oxidation kinetics, electron transfer to the anode, proton transfer from the anode to the cathode, and the oxygen reduction reaction (ORR) at the cathode [6]. Among these, the sluggish ORR kinetics is widely recognized as one of the major factors limiting overall PMFC performance. Oxygen is the most used electron acceptor in microbial fuel cells due to its high availability and environmentally friendly reduction product. Additionally, oxygen has a high redox potential of 1.23 V, allowing for higher energy output. However, the oxygen reduction reaction (ORR) is kinetically slow and requires a catalyst to accelerate the process [5]. Platinum-based catalysts exhibit excellent activity; however, their high cost and susceptibility to poisoning under environmental conditions have motivated intensive research into low-cost alternative catalysts [7]. Carbon-based materials such as graphite, carbon brushes, and graphene oxide are widely used for their high biocompatibility and surface area, which improve microbial activity and electron transfer [8].

In PMFC systems, effective electrode materials must be biocompatible, electrically conductive, and capable of promoting efficient ORR kinetics at the cathode. Both theoretical and experimental studies have demonstrated that heteroatom doping of graphene with elements such as N, B, S, or P can significantly modify its electronic structure and chemical reactivity, thereby improving its catalytic activity toward the ORR and offering a promising alternative to Pt-based catalysts in fuel cell applications [9]. Boron-doped graphene has been reported to exhibit enhanced electrocatalytic activity toward oxygen reduction and improved capacitive behavior compared with pristine graphene [10].

Most reported synthesis approaches for boron doping of graphene include chemical vapor deposition (CVD) and high-temperature thermal annealing using boron-containing precursors such as BCl_3 [11]. Although effective for achieving substitutional doping, these methods typically require elevated temperatures, toxic gaseous reagents, and specialized equipment, which limit their scalability and practical applicability. Therefore, the development of low-cost, scalable, and environmentally benign strategies for boron incorporation into graphene remains an important research focus.

Ultrasonication has recently emerged as a promising strategy for the modification and doping of graphene-based materials. This rapid and environmentally friendly process ensures homogeneous distribution of dopant atoms and allows precise control of doping levels without requiring high-temperature treatments or reducing atmospheres [9, 12, 13]. In particular, boric acid has been used as a boron source in aqueous GO suspensions, where ultrasonication enables efficient incorporation of boron into the graphene oxide structure under mild conditions [9, 12, 14].

Zhang et al. demonstrated that heteroatom incorporation into graphene oxide can be facilitated at temperatures as low as 5 °C with the aid of ultrasonication [9]. Their XPS analysis revealed the presence of boron-carbon and boron–oxygen–carbon bonding configurations (e.g., BC_2O and BCO_2) prior to high-temperature annealing, indicating that sonochemical effects can promote defect-associated boron interaction within the oxygen-rich GO structure. These findings indicate that low-temperature sonochemical processes can promote defect-associated boron bonding rather than purely physical adsorption [9].

In general, exfoliation is a process that separates layered materials, such as graphite, into thinner sheets like graphene. In electrochemical exfoliation, this is achieved by applying a voltage in an electrolyte solution with a two-electrode system. A graphite electrode acts as a sacrificial working electrode, while a counter electrode completes the electrical circuit. When voltage is applied, oxidation begins at the edges and grain boundaries of the graphite layers. Hydroxyl ions (OH^-) formed during the reaction, attack these edges and weaken the bonds between layers. Simultaneously, anions like sulfate ions (SO_4^{2-}) in the electrolyte intercalate between the layers, causing further separation. Parvez et al. found that salts containing anions, such as ClO_4^-, Cl^-, and NO_3^-, had no apparent exfoliation effects. It was seen that only expansion of the graphite electrode was observed when using ClO_4^- and NO_3^- anions. On the other hand, salts

containing sulfate anions in the form of sulfate-containing salts such as $(NH_4)_2SO_4$ exhibited pronounced exfoliation efficiency [15].

As the electrochemical exfoliation reaction proceed, gas evolution (such as SO_2 or O_2) helps expand and exfoliate the graphite into thin graphene sheets. The reactions that occur on the graphite layers can be seen in Eq. 3 to 7 [16]. :

$$C_s \underrightarrow{2H_2O} C_{s-1} + CO_2 + 4H^+ + 4e^- \quad (3)$$

$$C_b \underleftrightarrow{H_2O} C_bOH + H^+ + e^- \quad (4)$$

Table 1 Wastewater sources and their advantages and disadvantages

Wastewater type	Advantages	Disadvantages / Challenges	Ref.
Brewery wastewater	High organic load (sugars, organic acids) supports microbial activity and power generation; high COD removal and power density reported	Composition varies depending on brewery process; may contain inhibitory compounds; pretreatment sometimes required	[22, 23]
Domestic wastewater	Abundant, low-cost, and continuously available; enables simultaneous treatment and energy production	Often lower organic content compared to industrial wastewater → lower power density; contains suspended solids and pathogens	[22, 24]
Distillery wastewater	Rich in sugars and alcohol derivatives → excellent carbon source; high energy conversion potential	Often acidic and may contain toxic byproducts (e.g., phenols); pH control and pretreatment	[25]
Animal manure mixtures	Very high organic matter and nutrient content; cheap and widely available; supports microbial growth	High suspended solids → clogging risk; unpleasant odor; pathogens and high ammonia concentrations can inhibit microbial activity	[26]
Photosynthetic systems with real wastewater	Oxygen produced by photosynthesis reduces cathode limitations; synergy between plant/algal growth and wastewater treatment	Requires light input; typically lower power density compared to organic-rich wastewaters; system stability is challenging	[27]
Cheese whey wastewater	Rich in lactose, proteins, lactic acid, and minerals; enhances microbial activity and biofilm formation; improves PMFC efficiency; valorizes a problematic dairy byproduct	Very high organic load → if untreated, causes oxygen depletion in aquatic systems; variable composition depending on cheese process; requires dilution or controlled feeding	[19–21, 28]

$$C_b \underleftrightarrow{2H_2O} C_{b-1}COOH + 3H^+ + 3e^- \quad (5)$$

$$H_2O \rightarrow 2H^+ + \tfrac{1}{2}O_2 + 2e^- \quad (6)$$

$$C_bOH + H_2SO_4 \underleftrightarrow{H_2O} SO_4C_b + 2e^- \quad (7)$$

C_s, C_b in equations above denote surface of graphite electrode, and graphite bulk.

Compared with pure graphite, pencil graphite core is essentially a nanocomposite composed of graphite and intercalated clay particles with varying graphite-to-clay ratios [17]. The presence of nanoclay within the pencil core facilitates the exfoliation process by promoting interlayer separation during electrochemical treatment. Kunfeng et al. reported that nanoclay-assisted electrochemical oxidation in neutral $(NH_4)_2SO_4$ electrolyte enables efficient graphene separation of graphene from graphite pencil core [17]. Building on this concept, the present study employs pencil graphite as the starting material for the electrochemical exfoliation of graphene. Moreover, controlled electrochemical exfoliation of pencil lead has been reported to yield carbon-dominant graphene with indicating limited residual impurity contribution in the final product [18].

Motivated by this approach, the present study employs a low-temperature ultrasonic treatment to introduce boron species into electrochemically exfoliated graphene oxide and evaluates the resulting materials as anode and cathode catalysts in plant microbial fuel cells.

PMFC performance is also strongly influenced by the availability of organic substrates in the anode compartment. Table 1 summarizes various wastewater sources that have been applied in MFC and PMFC studies, highlighting their advantages and limitations. Cheese whey, an abundant agro-industrial byproduct, contains high levels of lactose, lactic acid, proteins, lipids, and mineral components [19]. Whey's organic ingredients have the potential to improve biological activity by enriching the soil microorganisms. Minerals like calcium and potassium supply vital nutrients that plants require and aid in controlling the ion balance in the soil. Whey can boost plant biomass and encourage root development in sugar beet plants, according to studies [20]. Previous studies have reported that organic loading and whey concentration significantly affect bioelectrochemical system performance. For example, Tremouli et al. demonstrated that varying cheese whey concentrations in microbial fuel cells led to notable differences in power output and system efficiency, indicating the existence of an optimal substrate concentration range [21].

Therefore, in this study it was aimed to develop a sustainable and cost-effective electrocatalyst for PMFC applications by integrating low-temperature ultrasonic boron incorporation with electrochemically exfoliated graphene oxide. The synthesized boron-doped graphene oxide materials were systematically evaluated as anode, cathode catalysts in plant microbial fuel cells. Furthermore, the effect of cheese whey supplementation as an external organic substrate was investigated to enhance bioelectrochemical performance. This combined strategy provides a scalable pathway for improving PMFC efficiency while simultaneously contributing to agro-industrial waste valorization and sustainable energy production.

2 Experimental

2.1 Chemical and Materials

All chemicals used in this study were of analytical grade and used as received without further purification. Boric acid (CAS: 10043-35-3) and potassium hydroxide (CAS: 1310-58-3) were obtained from Merck. Ammonium sulfate (CAS: 7783-20-2) was purchased from Carlo Erba Reagents. 8B-type graphite pencil and pure graphite rod (5.56 mm) were obtained from commercial sources. In addition, whey was purchased from Alfasol in powdered form to ensure long-term stability and to avoid changes in its physicochemical properties during the experimental period. Composition of whey (purchased from Alfasol) can be seen in Table 2. Before PMFC performance tests, 1% (w/v) aqueous solution of whey was freshly prepared and used as organic load for the PMFC system.

Whey typically exhibits an acidic pH (≈ 4–5) environment due to presence of lactic acid which could adversely affect both plant roots and rhizospheric microbial communities by acid stress if applied directly [29]. As emphasized in recent studies [30], substrate composition and pH regulation play a decisive role in maintaining microbial stability and ensuring efficient bioelectrochemical performance in environmental systems utilizing organic waste streams. Previous studies on dairy wastewater and whey valorization [31] in electrochemical and bioelectrochemical systems have also emphasized that uncontrolled pH conditions may inhibit microbial activity and negatively affect system performance. Therefore, in order to eliminate acidic stress as a variable and regulate pH in the PMFC system, prior to feeding whey was diluted as a 1 wt% aqueous solution and its pH was adjusted to neutral (pH ≈ 7.0) using a calibrated pH meter. This deliberate neutralization step ensured that the added substrate did not impose acidity into the soil environment or cause acid shock to the PMFC system.

Table 2 Cheese whey laboratory analysis

Composition	Amount % (w/w)
Fat	0.50
Ash	3.50
Salt	1.63
Protein (N*6.38)	7.01
Acidity (Lactic Acid)	0.11
Lactose	80.89

2.2 Graphene Oxide Synthesis

Synthesis of GO by electrochemical exfoliation was conducted with an 8B type graphite pencil working electrode. 8B type graphite pencil contains 90% graphite, 7% clay and 5% wax [32]. In exfoliation studies, it was observed that graphite pencils with lower clay content demonstrate superior electrochemical behavior during high-voltage exfoliation processes [13]. In addition to working electrode, pure graphite rod (5.56 mm) was selected as the counter electrode for the sink of electrons generated during oxidation of graphite pencil. 0.1 M ammonium sulfate ($(NH_4)_2SO_4$) solution was used as an electrolyte in the electrochemical cell. Pure graphite counter electrode and 8B type pencil graphite rod working electrode was positioned approximately 2 cm apart in the electrolyte solution. During the electrochemical exfoliation process, a constant voltage of 8 V was applied. When an 8 V potential is applied to the 8B pencil core in a sulfate-based electrolyte, electrochemical oxidation and intercalation selectively occur at the graphitic domains. As a result, defected graphene/graphene oxide sheets are exfoliated from the pencil core and spontaneously migrate toward the electrolyte surface, where they accumulate in the form of a light foam-like layer. During the exfoliation process the oxidized carbon material detached from the electrode and accumulated near the electrolyte surface in a foam-like form. In contrast, impurities originating from the pencil core, such as clay-based binders remained at the bottom of the reaction vessel due to differences in density, electrical conductivity, and electrochemical activity compared to exfoliated layers. The floating exfoliated material was carefully collected and washed several times with deionized water. Finally, the exfoliation yield was dried in an oven at 90 °C for 1 h [13]. Purified, exfoliated fraction was used for further boron incorporation and electrochemical characterization (Fig. 1).



Fig. 1 Graphene oxide synthesis process used in this study

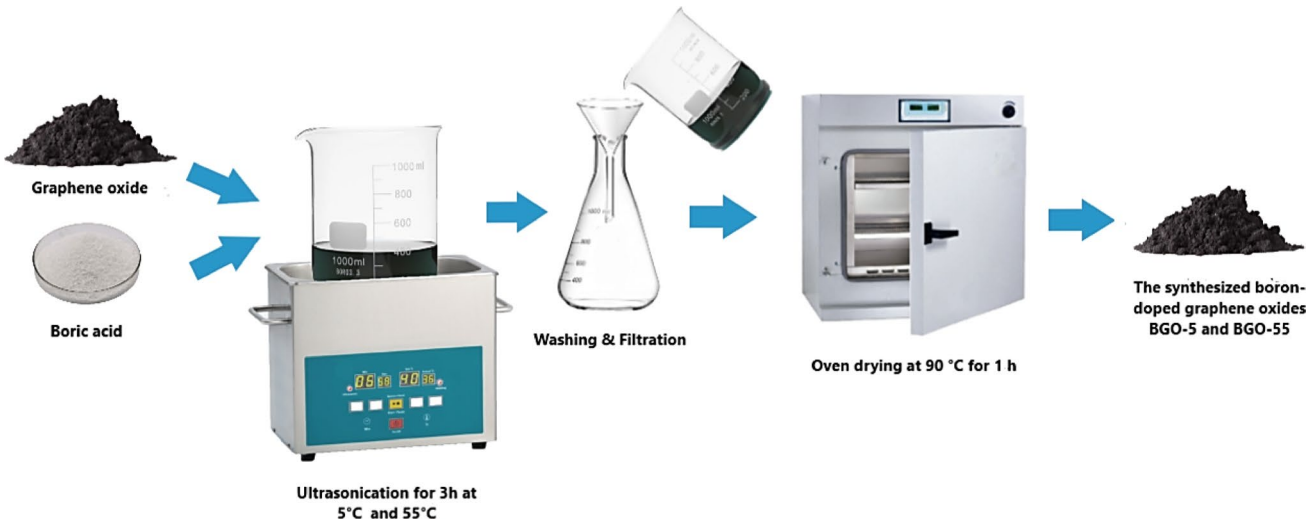


Fig. 2 Schematic illustration of the boron incorporation process applied to homemade graphene oxide in this study

2.3 Boron Incorporation in GO

To incorporate boron into homemade GO, ultrasonication technique was used as seen in Fig. 2. This method ensures that boron is evenly and homogeneously distributed into GO structure. For the ultrasonication process, boric acid solution was prepared with graphene oxide-water solution at a concentration of 2 mg/mL. Boric acid was used as the boron source in a 5:1(boric acid/GO) ratio by weight [12]. It was aimed to prepare electrocatalysts with two different boron loadings. To achieve two different boron loading percentages, the ultrasonication process was conducted at 5 °C and 55 °C for the attachment of boron atoms onto the GO surface [9]. Previous studies have demonstrated that ultrasonication temperature plays a critical role in the incorporation of heteroatoms into graphene oxide (GO). In particular, ultrasound-assisted boron codoping studies have shown that heteroatom incorporation can occur even at low bulk temperatures (≈ 5 °C) due to localized high-energy cavitation effects [9]. These cavitation events generate transient microenvironments with extremely high temperature and pressure, indicating that bulk solution temperature alone does not solely determine doping efficiency. Therefore, 5 °C was selected in the present study as a low-temperature reference condition to evaluate whether cavitation-driven effects are sufficient to promote boron incorporation under our experimental conditions. Conversely, increasing the bulk temperature to 55 °C provides additional thermal energy that enhances diffusion kinetics and facilitates more effective interaction between boron species and oxygen-containing functional groups or defect sites on GO during ultrasonication. Literature findings [9] further indicate that higher temperatures promote defect formation and increase the concentration of catalytically active boron configurations, such as graphitic boron (BC_3), which are beneficial for oxygen reduction reaction (ORR) activity. However, excessively high temperatures

may result in the loss of oxygen-containing groups and a decrease in defect density, potentially limiting doping efficiency. Accordingly, 55 °C was selected as a representative higher-energy condition to promote boron incorporation while avoiding structural degradation, thereby supporting a comparative temperature approach rather than an extensive temperature optimization study.

Synthesis mixture was processed in an ultrasonic bath for 3 h at the selected temperatures. Boron incorporated samples obtained at 5 °C and 55 °C were denoted as BGO-5 and BGO-55.

2.4 Spectroscopic Characterizations

Homemade electrocatalysts were characterized by using Raman Spectroscopy and Inductively Coupled Plasma Optical Emission Spectrometry (ICP-OES) to analyze boron incorporation in the GO structure and determine boron loading in the bulk GO. Raman Spectroscopy was performed with Renishaw inVia Dispersive Raman Spectrometer in Middle East Technical University (METU) Central Laboratory. ICP-OES analysis was conducted with Thermo Scientific model ICAP 7000 in Turkey Energy, Nuclear and Mineral Research Agency Boron Research Institute (TENMAK BOREN).

2.5 Electrochemical Measurements

Three electrode systems were used to carry out electrochemical characterizations of homemade electrocatalysts. Ag/AgCl reference electrode, a platinum counter electrode, and a glassy carbon working electrode were used in a three neck pyrex glass electrochemical cell. For the preparation of catalyst loaded working electrode, 6 mg of homemade catalyst was dispersed into 100 µL of deionized water and 100 µL of a 5 wt% Nafion solution (in alcohol). Prepared catalyst ink was loaded on the glassy carbon electrode and then the electrode was dried under hot air fan for 5 min. Initially, cyclic voltammetry (CV) was conducted in the electrochemical cell in the potential range of -1.0 to 0.0 V (vs. Ag/AgCl) at various scan rates of 10, 20, 50, and 100 mV/s with a bipotantiostat (model AFCBP1 Pine Research). Electrochemical capacitance of homemade electrocatalysts were determined from CV curves in the non-faradaic region at different scan rates. By ploting current as a function of scan rate, capacitance values were extracted from the slopes of linear relation between current vs. scan rate. Secondly, electrochemical impedance spectroscopy (EIS) analysis was carried out with potantiostat (Reference 600 Gamry Instruments) in the frequency range of 1 MHz to 0.5 Hz with an amplitude of 10 mV. EIS measurements were conducted at different negative applied potentials of -1.1 V and −0.6 V vs. Ag/AgCl. Nyquist plots from EIS were fitted using an equivalent circuit model to extract charge transfer resistance (Rp) for homemade electrocatalysts. All measurements were conducted in an O_2 saturated 0,1 M KOH electrolyte.

Table 3 Experimental 2 × 3 design of PMFC

Experiment No	Catalyst Type	Catalyst Location
1	GO	Anode
2	GO	Cathode
3	BGO-5	Anode
4	BGO-5	Cathode
5	BGO-55	Anode
6	BGO-55	Cathode

2.6 PMFC Set-Up and Performance Tests

2 × 3 factorial experimental design as seen in Table 3 was employed to evaluate the effect and allocation of electrocatalyst types on PMFC performance. The two studied factors were: (i) homemade catalyst type (GO, BGO-5, BGO-55) and (ii) electrocatalyst allocation (anode or cathode). This factorial design resulted in six experimental PMFC systems in total.

PMFC system was constructed using sugar beet plants grown in six soil-based pots with dimensions of approximately 12 cm in diameter and 10 cm in depth. Sugar beet seeds were sown in November, germination occurred in December in lab environment, and adequate root development and rhizosphere maturation required waiting until April.

Graphite rod cathode electrodes were placed on the soil surface to ensure sufficient oxygen source, whereas the graphite rod anode electrodes were positioned close to the plant roots (in the region of rhizosphere) to facilitate interaction with root exudates. Once the plants reached the appropriate growth stage, homemade catalysts were deposited onto either the anode or the cathode electrode compartments depending on the configuration at a loading of 4 mg cm^{-2}. All experiments were conducted under controlled laboratory conditions with a continuous full-spectrum LED light source 14 h/day and at an average ambient temperature of 24 °C. Electrochemical measurements were performed during four months after plant cultivation.

Electrocatalyst activities in six (single sugar beet units) PMFC compartments (seen in Fig. 3) were monitored for 60 days after 4 months of plant growth stage (after sowing). Whey feeding was introduced on day 19. 1 wt% 50 ml whey aqueous solution was prepared and fed into each PMFC in batch mode throughout the experiments.

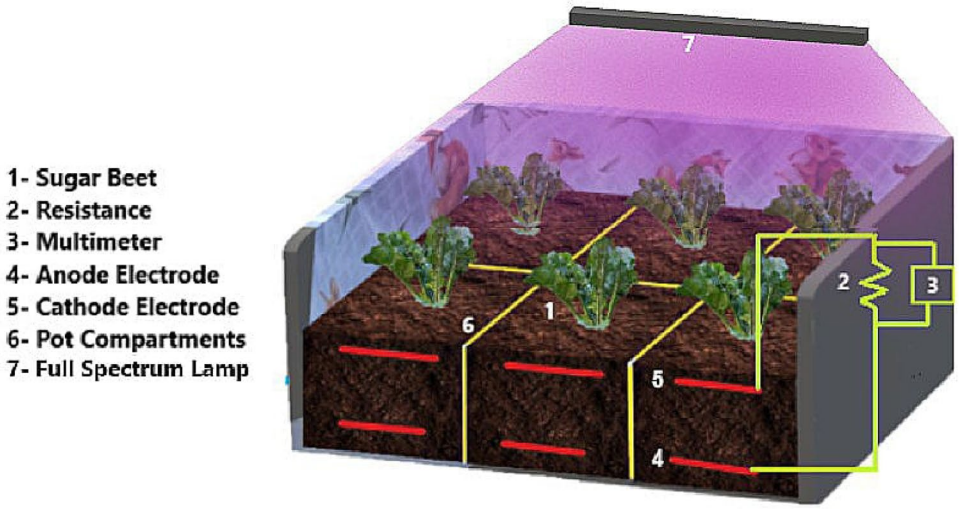


Fig. 3 Plant based microbial fuel cell set consisting of six compartments

Table 4 ICP-OES Analysis results of boron loading level at ppm

Sample	B (ppm)
BGO-5	200.7
BGO-55	651.1

To test the electrochemical performance of homemade electrocatalysts in PMFC set up seen in Fig. 3, polarization tests were carried out by measuring the steady-state cell current and cell potential at variable cell resistances of 50, 100, and 150 kΩ. In addition, open-circuit potential of PMFC was also monitored regularly before and after whey loading.

3 Results and Discussion

3.1 Inductively Coupled Plasma Optical Emission Spectrometry

Boron content of the samples was quantified by ICP-OES. As seen in Table 4, boron incorporation in GO was seen to be successful and was more efficient with the increase of ultrasonication temperature.

3.2 Raman Spectroscopy

Defects and the graphene layers of electrocatalysts were analyzed by Raman spectroscopy. Raman spectra of the graphite powder (from 8B-type graphite pencil) which is denoted as G, homemade graphene oxide, GO, homemade boron incorporated graphene catalysts, BGO-5 and BGO-55 samples were shown in Fig. 4.

Raman spectra in Fig. 4 shows three main peaks, which correspond to D(~1350 cm^{-1}), G(~1575 cm^{-1}) and 2D (~2700 cm^{-1}) bands in the 0–3500 cm^{-1} range. G band corresponds to the in-plane stretching vibration of sp^2-bonded carbon atoms, whereas the D band intensity (I_D) reflects the degree of structural defects within the graphene layers. Therefore, I_D/I_G is related with the density of structural defects in the graphene. The I_D/I_G ratios reported in the literature from graphene oxide

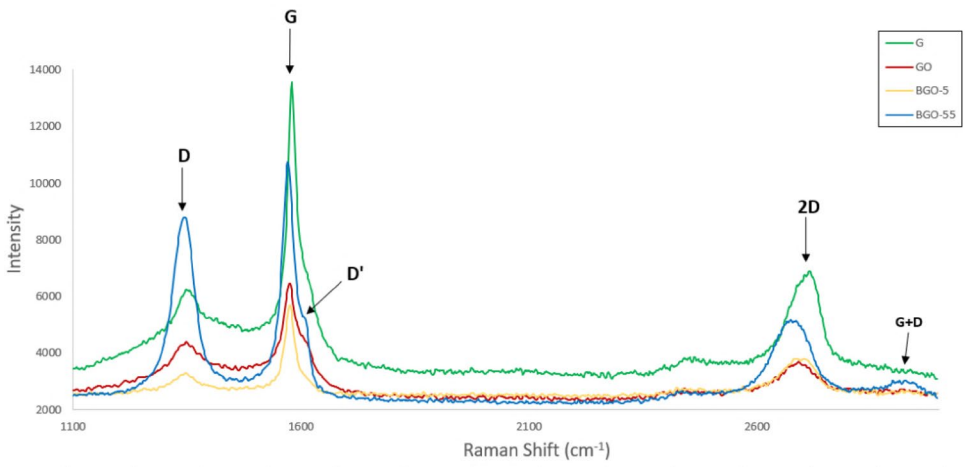


Fig. 4 Raman spectra of the homemade electrocatalysts: G (pencil core), GO, BGO-5, and BGO-55

Table 5 Graphene oxide synthesis by electrochemical exfoliation in the literature

Working Electrode	Counter Electrode	Electrolytes	Applied potential (V)	I_D/I_G	References
Graphite rod	Pt	0.5M H_2SO_4	5 V	0.36	[33]
Graphite rod	Pt	0.5M H_2SO_4	10 V	1.16	[33]
5B pencil core	Graphite flake	0.1 M $(NH_4)_2SO_4$	10 V	< 1.0	[17]
6B rod pencil	6B rod pencil	0.1 M $(NH_4)_2SO_4$	8 V	0.46	[13]
Pencil core (pencil type unspecified)	Pencil Core (pencil type unspecified)	(H_2SO_4 or H_3PO4)	1–7 V	0.71	[34]
Graphite flakes	Graphite foil	0.1 M $(NH_4)_2SO_4$	10 V	0.9–1.2	[35]
Graphite foil	Graphite foil	1.0M H_2SO_4	3 V	0.16	[36]
Graphite rod	Pt	0.2 M $(NH_3)_2SO_4$	10 V	1.76	[37]

Table 6 Band positions and intensity ratios from Raman spectra

Sample	G Band (cm^{-1})	D Band(cm^{-1})	2D Band(cm^{-1})	I_D/I_G
G	1580	1348	2720	0.46
GO	1576	1349	2693	0.68
BGO-5	1576	1347	2696	0.58
BGO-55	1572	1347	2689	0.82

synthesized using different working, counter electrode materials, inorganic electrolytes and applied potentials are presented in Table 5. In Table 5, I_D/I_G ratios range between 0.16 and 1.76 from graphite foil to graphite rod.

In Figs. 4 and 8B pencil core graphite powder sample shows two main peaks which are G band at 1580 cm^{-1} and a weak D band at 1348 cm^{-1} related to structural defects. Low I_D/I_G ratio of 0.46 shown in Table 6 indicates that the pencil core has a highly ordered graphitic structure. After electrochemical exfoliation, GO sample exhibited a higher I_D/I_G ratio of 0.68 which suggests that oxidation introduced more structural defects and oxygen-containing functional groups, confirming the disruption of the sp^2 domains during exfoliation.

In the boron incorporated sample, BGO-55, shown in Table 6, I_D/I_G ratio is even higher with a value of 0.82 which indicates the existence of oxygen functional groups or boron incorporation generating additional defect sites and lattice distortions, at higher temperature [38–41]. 2D band intensity of BGO-55 higher than the GO and the appearance of the D′ band could indicate that boron incorporation was successful in graphene altering the electronic structure and introducing defects and structural disorder [42]. In addition, appearance of G + D band around 2950–3000 cm^{-1} specific to BGO-55 is also known to originate from defect-related vibrations in the graphene lattice [43–45]. It should be noted that although 2950–3000 cm^{-1} band could correspond to C–H stretching vibrations originating from hydrocarbon residues, which is a reasonable concern given that commercial pencil leads may contain wax-based binders, Raman spectra do not not support the interpretation of this band as residual wax contamination. Because, if the 2900–3000 cm^{-1} feature were derived from hydrocarbon-based C–H stretching vibrations, it should also be observable in the pristine pencil graphite sample (G), which directly contains wax and clay additives. Furthermore, since GO and BGO-5 were synthesized from the same precursor and subjected to identical exfoliation, washing, and drying procedures, the same hydrocarbon-related signal would be expected in those samples as well. Importantly, this band is absent in G, GO, and BGO-5 and appears exclusively in BGO-55. If residual wax were responsible, the peak would not selectively emerge only after boron treatment at 55 °C. The fact that it is observed solely in BGO-55 argues against a hydrocarbon impurity origin. In addition, the structural evolution observed in Raman analysis further supports this interpretation. The increase in ID/IG ratio is detected only in BGO-55. Neither ultrasonication alone (GO), nor the pristine graphite (G), nor boron treatment at 5 °C (BGO-5) resulted in an increased ID/IG value suggesting an indicator of defect density due to boron incorporation. If ultrasonication-induced mechanical damage were the dominant factor, a similar increase would also be expected in GO and BGO-5, which were subjected to the same sonication process. The absence of such an increase in these samples indicates that mechanical defect generation alone cannot explain the observed structural changes. Instead, the selective rise in ID/IG correlates with the higher boron content confirmed by ICP-OES in BGO-55, suggesting that boron treatment at elevated temperature induces additional lattice perturbation or defect formation beyond sonication effects. Taken together, these correlated findings support the assignment of the observed spectral feature to boron-associated structural modification or boron defect-activated combination modes rather than residual wax-derived C–H vibrations.

3.3 Electrochemical Characterizations

Electrochemical behavior of homemade electrocatalysts and unloaded glassy carbon electrode was evaluated with cyclic voltammetry in the potential range between − 1.0 and 0.0 V (vs. Ag/AgCl electrode) which was shown in Fig. 5. Significant increase in capacitance and oxygen reduction current at ~-0.3 V was observed for the

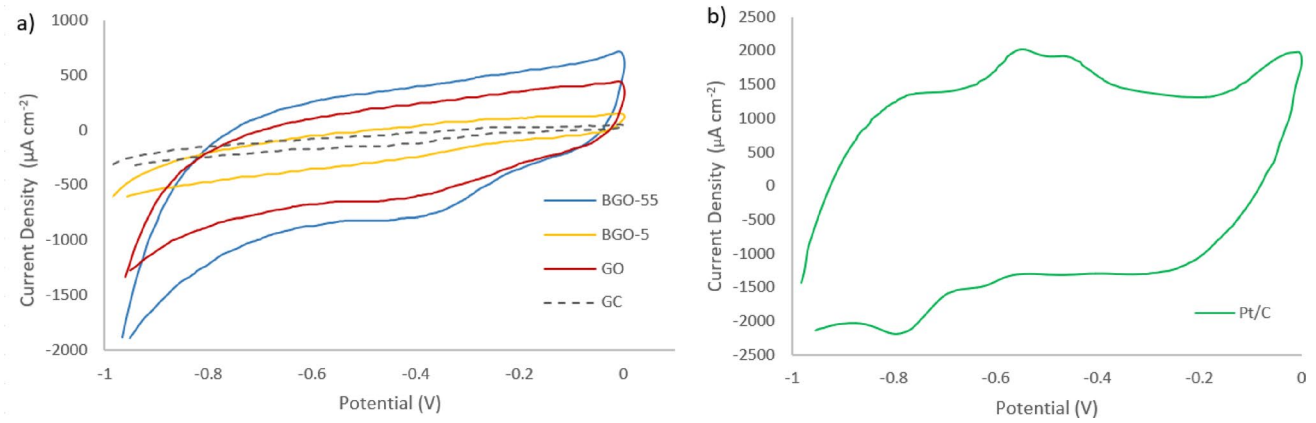


Fig. 5 Cyclic voltammograms of homemade electrocatalysts and GC in air saturated 0.1 M KOH electrolyte at a scan rate of 20 mV/s. a) Homemade catalysts and GC reference, b)Pt/C (20 wt% Pt) reference

BGO-55 electrode. The presence of this oxygen reduction peak suggests that higher boron incorporation in BGO-55 could have significantly improved ORR electrocatalytic activity and enhanced electron transfer kinetics. It should be pointed out that no baseline correction was applied to the CV curves. All measurements were recorded under identical experimental conditions, and the data are presented in their raw form. In our experimental configuration, the glassy carbon (GC) electrode without catalyst loading was used as the reference baseline electrode. The apparent crossover or higher current density observed for bare GC in certain potential regions does not indicate inconsistency in electrode preparation. Rather, it could arise from differences in double-layer capacitance and surface morphology. Catalyst loading can partially block the intrinsic capacitive response of the GC surface or alter charge storage behavior depending on film thickness, dispersion quality, and conductivity. In some potential regions where no faradaic process dominates, capacitive contributions may therefore differ between bare GC and catalyst-coated electrodes, leading to localized current crossover. Importantly, the electrocatalytic evaluation was not based on absolute current magnitude across the entire scan window, but specifically on the potential region associated with oxygen reduction behavior.

To provide a meaningful reference, we have also performed CV measurements on commercial Pt/C under the same experimental conditions. Pt/C exhibited strong capacitive currents arising from the high surface area carbon support, which largely masked the ORR peak around approximately − 0.2 V vs. Ag/AgCl. This behavior is consistent with literature reports describing significant double-layer charging currents in supported Pt catalyst compared to polycrystalline Pt disc under similar conditions [46]. At potentials more negative than − 0.4 V vs. Ag/AgCl, a slight hydrogen underpotential deposition region was also observed for Pt/C. Therefore, under our non-RDE (or without hyrodynamic effect) or stagnant conditions, even Pt/C did not display a ORR peak. On the other hand, when compared to other home made catalysts under identical conditions, BGO-55 exhibited a discernible reduction feature centered around approximately − 0.3 V vs. Ag/AgCl. Although this peak is broad and partially masked by capacitive contributions (as also observed, to a lesser extent, for the homemade catalysts compared to Pt/C), it is more pronounced than that of GO, BGO-5, and bare glassy carbon. Thus, our claim is not that BGO-55 approaches polycrystalline Pt performance, but rather that it demonstrates relatively improved ORR activity within the series of materials investigated in this study.

Electrochemical impedance spectroscopy (EIS) measurements were performed at − 0.6 V and − 1.1 V (vs. Ag/AgCl) in 0.1 M KOH solution corresponding to different electrochemical processes. Applied potential of − 0.6 V lies within the oxygen reduction region, while − 1.1 V falls into the hydrogen evolution region which provide valuable insight into the charge transfer kinetics. Nyquist plots corresponding to glassy carbon (GC) and homemade electrocatalysts can be seen in Fig. 6a. It was seen that Nyquist arcs shrink significantly on boron incorporated graphene oxide electrocatalysts. After fitting the equivalent circuit (constant phase element with diffusion) (Fig. 6c) to the Nyquist plots by Gamry software, solution resistance (Ru), charge transfer resistance (Rp), warburg impedance (W) and equivalent capacitance (Y0) and α values were extracted. The Y0 value represents the pseudo-capacitance of the Constant Phase Element (CPE) in Siemens.sα where α is the exponent of constant phase element ranging between 0 and 1 indicates non ideal behavior of capacitive element. Constant

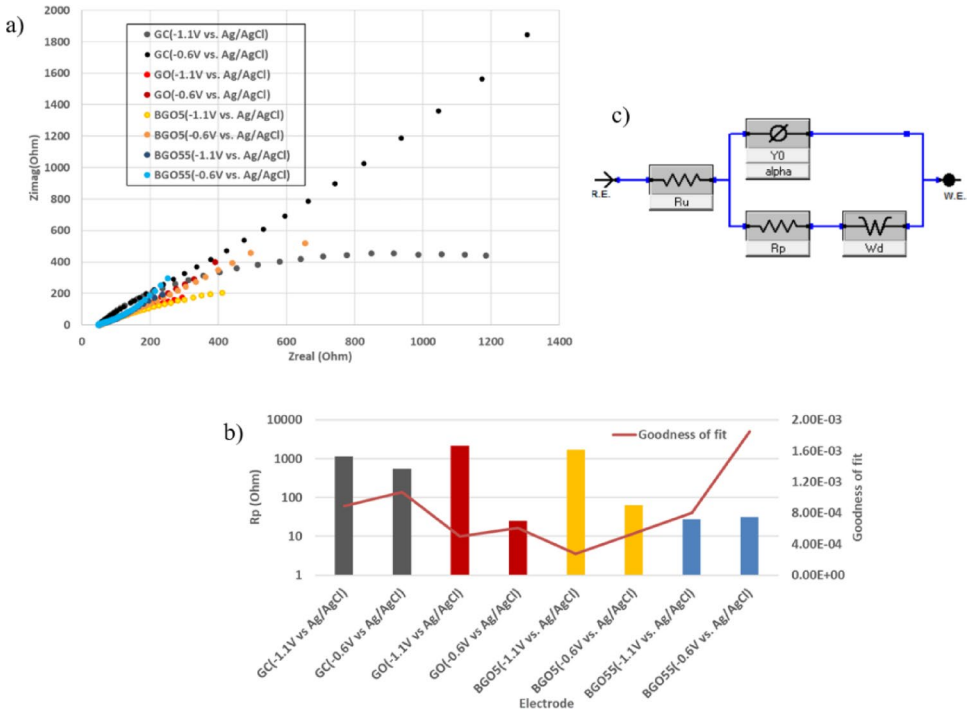


Fig. 6 (a) Nyquist plots of home-made electrocatalysts and GC electrode (b) Comparison of charge transfer resistance (Rp) values extracted from equivalent circuit (c) Equivalent circuit (constant phase element with diffusion) used for extraction of EIS parameters

Table 7 Extracted parameters at different applied potentials from the equivalent circuit model

	Model	Rp (Ohm)	Ru (Ohm)	Y0 ($S.s^{\alpha}$)	α	W ($S.s^{1/2}$)	Goodness of fit
GC (-1.1 V vs. Ag/AgCl)	CPE with diffusion	1155.00	50.72	9.29E-05	7.13E-01	1.40E-03	8.92E-04
	CPE	1487	50.2	116E-6	681.6E-3		1.7E-3
GC (-0.6 V vs. Ag/AgCl)	CPE with diffusion	546.50	49.55	1.02E-04	6.95E-01	1.43E-04	1.07E-03
	CPE	29.01E3	48.21	206.8E-6	604.1E-3	-	2.28E-3
GO (-1.1 V vs. Ag/AgCl)	CPE with diffusion	2143.00	51.03	1.78E-03	4.38E-01	1.23E-03	5.00E-04
	CPE	3002	50.96	1.82E-3	433.7E-3	-	5.03E-4
GO (-0.6 V vs. Ag/AgCl)	CPE with diffusion	24.58	51.10	1.47E-04	6.58E-01	1.08E-03	6.11E-04
	CPE	2.05E9	51.43	1.28E-3	478E-3	-	1.52E-3
BGO5 (-1.1 V vs. Ag/AgCl)	CPE with diffusion	1693.00	52.05	1.16E-03	4.39E-01	2.81E+01	2.75E-04
	CPE	1693	52.05	1.16E-3	4.39E-1	-	2.75E-04
BGO5 (-0.6 V vs. Ag/AgCl)	CPE with diffusion	62.79	52.02	3.94E-04	5.11E-01	4.11E-04	5.34E-04
	CPE	3.59E9	53.06	856.2E-6	467.7E-3	-	1.19E-3
BGO55 (-1.1 V vs. Ag/AgCl)	CPE with diffusion	27.88	50.29	2.61E-03	6.58E-01	1.98E-03	8.05E-04
	CPE	5.55E9	50.22	2.34E-3	447.8E-3	-	2.03E-3
BGO55 (-0.6 V vs. Ag/AgCl)	CPE with diffusion	30.99	48.68	3.43E-04	6.17E-01	1.32E-03	1.85E-03
	CPE	1.36E9	49.1	1.7E-3	481.8E-3	-	3.3E-3

phase element is used to model electrochemical capacitor instead of a pure electrical capacitor (where α is equal to 1) to account for the non homogeneous, porous and rough electrochemical interface and distribution of time constants or variation of electrochemical properties on the electrode surface [47–49]. Ru indicates uncompensated electrolyte solution resistance between reference and working electrode in the electrochemical cell. Rp represents kinetic resistance of the reduction reactions at the porous electrode. Variation in Rp indicates the change in the speed of electron transfer. Warburg Impedance (W) represents the diffusion of ions from the bulk electrolyte to the porous electrode surface [50]. In our case, the "Warburg tail" could be most likely overlapped by the large Rp of the depressed semicircle, but it was a mathematical necessity for an accurate fit. To ensure the most accurate physical representation, we compared our original model with a simpler equivalent circuit consisting only of Ru, Rp and CPE (Y0, α). Therefore, the best fitted model was selected among CPE and CPE with diffusion model based on goodness of fit. Comparison of fitted parameters and goodness of fits of two models were given in Table 7.

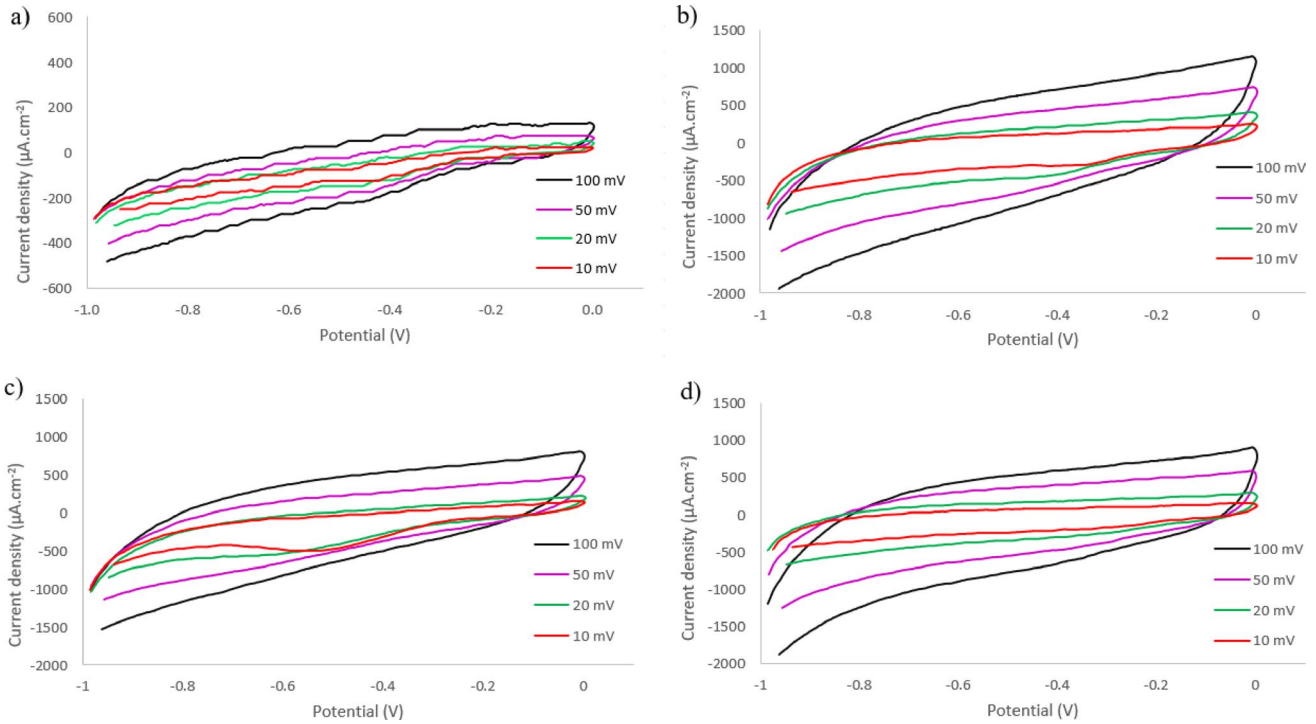


Fig. 7 Capacitance measured at scan rates of 10, 20, 50, 100 mV/s of (a) GC, (b) GO, (c) BGO-5, (d) BGO-55 in air saturated 0.1 M KOH electrolyte

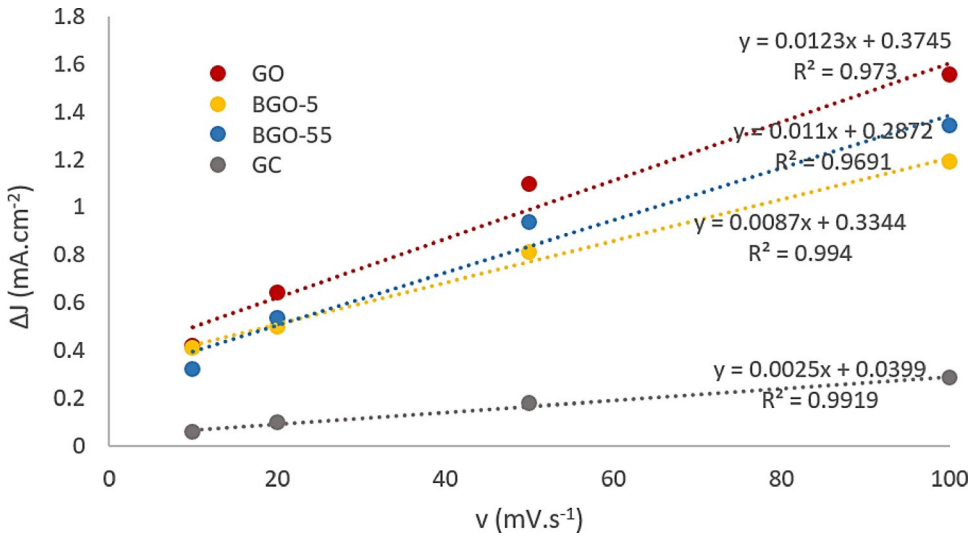


Fig. 8 Delta current density versus scan rates for capacitance calculation for homemade catalysts

When the extracted charge transfer resistances were compared in Fig. 6b, it was seen that BGO-55 demonstrated significantly lower Rp values at both −0.6 V and −1.1 V. These lower Rp values indicate that BGO-55 facilitates both oxygen reduction and hydrogen evolution electrokinetics. This enhanced electron transfer kinetics on BGO55 agrees well with the reduction currents seen in Fig. 5.

The electrochemical properties glassy carbon electrode and all prepared electrocatalysts were also evaluated by cyclic voltammetry at different scan rates (10-100mV/s) as seen in Fig. 7. Since electrochemical performance is also related to the electroactive surface area and thus to the double-layer capacitance of the samples, double layer capacitance values were determined by plotting current density difference at 0.6 V in the non-faradaic region in cyclic voltammograms in Fig. 7 plotted against scan rate. Double layer capacitance is defined by half of slope of the linear fits in Fig. 8. Double layer capacitances of GO, BGO-55, BGO-5 and GC were determined to be 6150, 5500, 4350 and 1250 μF/cm^2 respectively which shows the superior electrochemical active area of BGO-55.

3.4 PMFC Performance Tests

As summarized in Table 8, power densities in PMFC systems are reported. Higher values are generally observed in wetland-based PMFC systems employing oxygen-reducing biocathodes and enhanced oxygen diffusion, such as the wetland tubular configuration reported by Wetser et al., where power densities up to 82 mW m^{-2} were achieved under pure O_2 diffusion conditions [51]. In contrast, soil-based pot-type PMFCs operating without forced oxygen supply typically exhibit lower power densities. In this study the BGO-55 catalyst achieved competitive power densities, highlighting the catalytic contribution of boron-doped graphene oxide in enhancing electrochemical performance.

To evaluate the bioelectrochemical activities of homemade electrocatalysts (GO, BGO-5 and BGO-55) on either cathode or anode compartments, open circuit potential (OCP), soil resistance, cell potentials under 50,100,150 kΩ variable resistance, current density and power density were monitored for 60 days. Whey feeding was initiated on day 19 following the measurements on day 18, while post-feeding electrochemical measurements were first recorded on day 22. It should be noted that the reported OCP and power density values represent single-day steady- state measurements rather than averaged data from parallel biological replicates. For each measurement, the external resistance was connected and the system was allowed to stabilize for approximately 5 min before recording voltage and current values to ensure steady-state conditions.

Open circuit potentials (OCP) and soil resistances in the PMFC compartments were shown in Fig. 9. It can be seen from Fig. 9 that anode and cathode electrodes loaded with BGO55 shows significant increase in OCP and soil resistance. This significant increase was more apparent for anode electrode loaded with BGO55 especially after whey solution loading. The behavior at the anode electrode indicates the effect of boron incorporation on the oxidation of organic substrates by the electrogenic bacterial environment in the rhizosphere increased by whey loading. Unlike anode electrode loaded with BGO55, OCP profile become stable after the 30th day.

Table 8 Comparison of representative PMFC systems reported in the literature

System type	Reactor configuration	Plant	Electrode material (anode/cathode)	Catalyst	Substrate	Max power density (mW m^{-2})	Ref.
Soil-based PMFC	Pot-type system	Chlorophytum comosum	Graphite sheet	None	Rhizodeposition (no external substrate)	18	[52]
Soil-based PMFC	Pot-type system	Chasmanthe floribunda	Graphite plate	None	Rhizodeposition (no external substrate)	0.21	[52]
Soil-based PMFC	Pot-type system	Papyrus diffusus	Graphite plate	None	Rhizodeposition (no external substrate)	1.083	[52]
Soil-based PMFC	Pot-type system	Vigna radiata	Stainless steel mesh	None	Rhizodeposition (no external substrate)	0.35	[53]
Soil-based PMFC	Pot-type system	Vigna radiata	Graphite rods	None	Rhizodeposition (no external substrate)	0.12	[53].
Wetland PMFC	Constructed wetland box	Spartina anglica	Activated carbon + marine sediment / Graphite felt	None	Marine sediment organic matter (no external substrate)	1.04	[54]
Wetland PMFC (peat soil)	Tubular system	Phragmites australis	Graphite felt	Oxygen-reducing biocathode	Natural peat soil organic matter (no external substrate)	21	[51]
Wetland PMFC (salt marsh)	Tubular system	Spartina anglica	Graphite felt	Oxygen-reducing biocathode	Natural marine sediment organic matter (no external substrate)	82*	[51]
Soil-based PMFC (wetland soil)	Container system	Pennisetum alopecuroides	Carbon felt	None	Natural wetland soil (no external substrate)	2.86	[55]
Soil-based PMFC (wetland soil)	Container system	Typha angustifolia	Carbon felt	None	Natural wetland soil (no external substrate)	0.71	[55]
Soil-based PMFC	Pot-type system	Beta vulgaris	Graphite rod	BGO-55 (Anode-loaded)	Whey Wastewater + Rhizodeposition	0.94	This work
Soil-based PMFC	Pot-type system	Beta vulgaris	Graphite rod	BGO-55 (Cathode-loaded)	Whey Wastewater + Rhizodeposition	0.97	This work

* The maximum power density of 82 mW m^{-2} reported for Wetser et al. (2017) was obtained under pure O_2 diffusion conditions

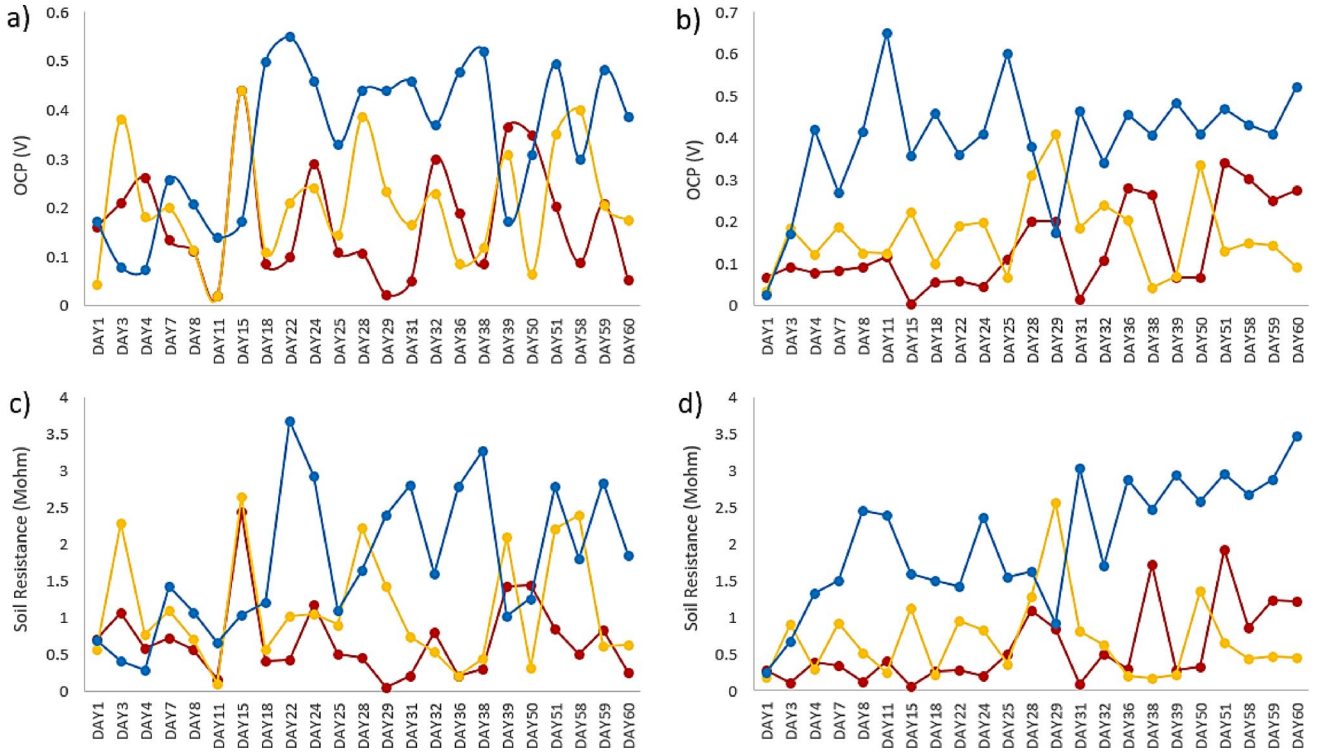


Fig. 9 OCP variation with respect to time for (a) anode electrode+catalyst-loaded PMFCs, (b) cathode electrode+catalyst-loaded PMFCs, and the soil resistance variation with respect to time for (c) anode electrode+catalyst-loaded PMFCs, (d) cathode electrode+catalyst-loaded PMFCs curves over a 60-day experimental period. The colors represent different catalysts: Red = GO, Yellow = BGO-5, and Blue = BGO-55

OCP oscillations in PMFC compartments are most probably associated with variations in the type of substrate utilized by electrogenic bacteria. The observed oscillatory behavior is characteristic of soil-based PMFC systems and is attributed to dynamic variations in rhizosphere microbial activity, substrate distribution, moisture content, and plant physiological fluctuations over time [56, 57].

Polarization curves of 6 PMFC compartments loaded with GO, BGO-5, and BGO-55 catalysts on day 59 and 60 for each PMFCs under different resistance loads were shown in Fig. 10. The polarization curves were recorded on days 59 and 60 because these corresponded to the operational period during which the systems exhibited their highest and most stable power density outputs. PMFC potential decreases with increasing current density for all compartments due to irreversible losses. Among the tested materials, BGO-55, either on the cathode or anode compartment exhibited lowest polarization and highest maximum power density. This PMFC performance confirms that boron incorporation significantly improved the electrocatalytic activity of both cathode and anode electrode.

Power densities of 6 PMFC compartments under 50 kΩ load were also monitored for 60 days before and after whey loading on day 22 (Fig. 11). The arrow indicates the onset of whey feeding (day 19), located between the measurements performed on days 18 and 22. As shown in Fig. 11, PMFC compartments exhibited low power densities until whey feeding was initiated on day 19, while a noticeable performance change was observed starting from day 22.

In the anode-catalyst systems Fig. 12a, power density exhibited a delayed increase, with a pronounced rise observed only after whey addition. As no ORR catalyst was employed at the cathode, the factors influencing power generation were primarily the metabolic activity of the electroactive bacteria and the electrical conductivity of the anode. The sharp increase following whey supplementation corresponded to the rise in available organic matter, which stimulated anodic biofilm activity. Among the tested anode materials, after whey supplementation BGO-55 consistently produced the highest power densities (increasing from 0.08 to 0.936 mW m^{-2}) and displayed superior performance compared to GO and BGO-5. These results indicate that boron incorporation enhanced the conductivity of the anode material, thereby positively impacting overall power output.

In the cathode-catalyst-loaded systems (Fig. 11b), no modification was applied to the anode, allowing the

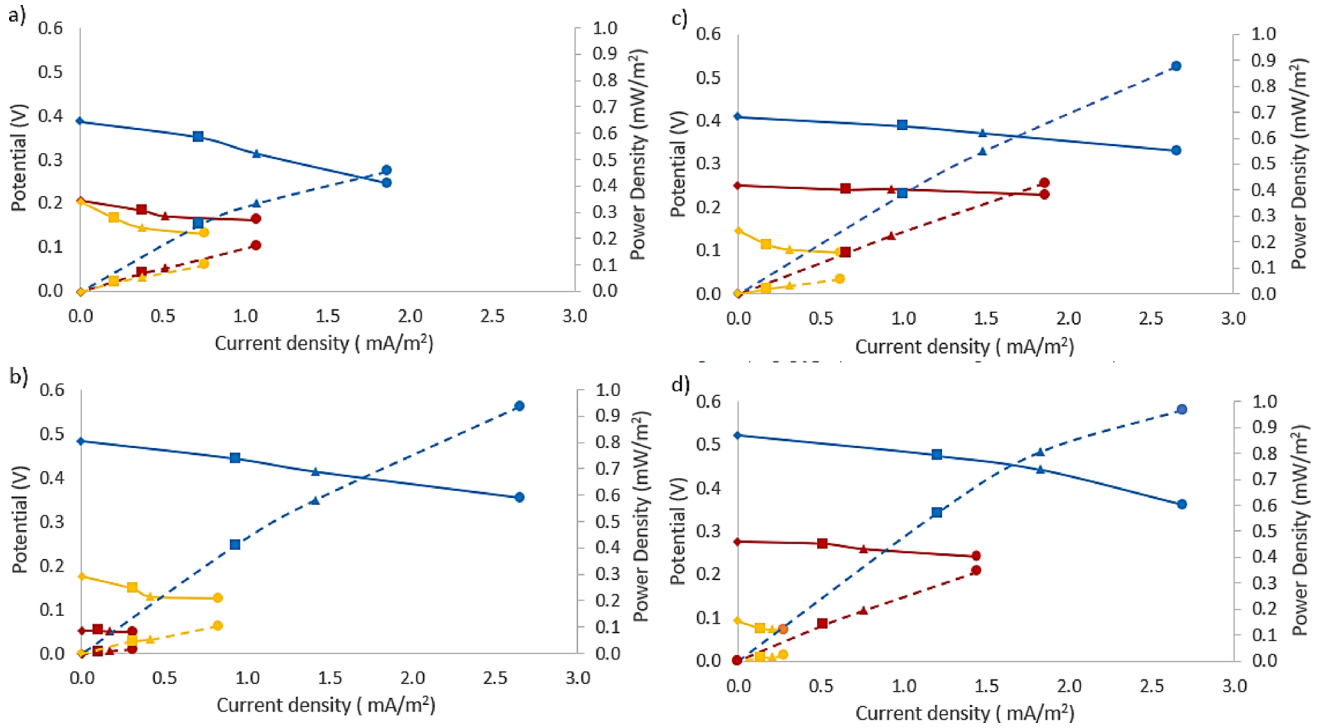


Fig. 10 Polarization curves of the (a) anode electrode+catalyst-loaded PMFCs obtained on the day 59, (b) anode electrode+catalyst-loaded PMFCs obtained on the day 60, (c) cathode electrode+catalyst-loaded PMFCs obtained on the day 59, (d) cathode electrode+catalyst-loaded PMFCs obtained on the day 60. Solid lines represent the potential as a function of current density, while dashed lines correspond to the power density. The symbols represent different external resistances: ■ = 150 kΩ, ▲ = 100 kΩ, and ● = 50 kΩ, ♦ = 0 kΩ. The colors correspond to the catalyst types: Red = GO, Yellow = BGO-5 and Blue = BGO-55

isolated evaluation of cathodic effects. Upon introduction of BGO-55 at the cathode compartment, examination of the power density profiles revealed that power generation began to increase even before whey supplementation and earlier than anode modified systems(anode compartment loaded with catalyst) This result confirms that sluggish oxygen reduction reaction (ORR) kinetics represented the primary limiting factor in PMFC performance and cathodic polarization losses were lower with BGO-55 loaded cathode compartment configuration.

Among the tested cathode catalysts, BGO-55 exhibited the highest power output after whey supplementation, with power density increasing from 0.558 to 0.967 mW m^{-2}. This superior performance is attributed to the enhanced catalytic activity of the boron-modified graphene oxide structure.

Under whey feeding conditions from Day 22 to Day 60, BGO-55 exhibited the highest average power density, reaching 0.616 mW m^{-2} at the anode and 0.663 mW m^{-2} at the cathode, outperforming both GO and BGO-5 electrodes. The maximum power density achieved by BGO-55 was 0.936 mW m^{-2} at the anode and 0.967 mW m^{-2} at the cathode. Raman analysis showed that the I_D/I_G ratio increased from 0.68 in GO to 0.82 in BGO-55, while ICP-OES confirmed a significantly higher boron content of 651.1 ppm in BGO-55 (as was shown in Table 4). These results indicate that higher boron incorporation leads to increased defect density, more active sites and electronic structure perturbation which enhance overall PMFC performance through anodic and cathodic electrochemical reaction kinetics. In fact, such boron-induced defect sites are known to modify local charge distribution and facilitate oxygen adsorption and electron transfer during ORR. At this point, it should be also pointed out that although definitive assignment of substitutional boron doping was not conclusively established by ICP-OES analysis and Raman spectrocopy, several observations suggest that the boron present in BGO-55 is unlikely to be physisorbed. Raman spectroscopy reveals a temperature-dependent structural evolution, with BGO-55 exhibiting a significantly higher I_D/I_G ratio compared to pure GO, indicating enhanced defect density and lattice perturbation. Such pronounced structural modification would not be expected from simple surface adsorption alone. Moreover, the increased defect density due to boron incorporation correlates well with reduced charge-transfer resistance and enhanced ORR activity, as demonstrated by EIS and CV analyses. The consistent relationship between boron content, defect enrichment, and electrochemical improvement supports defect-associated boron

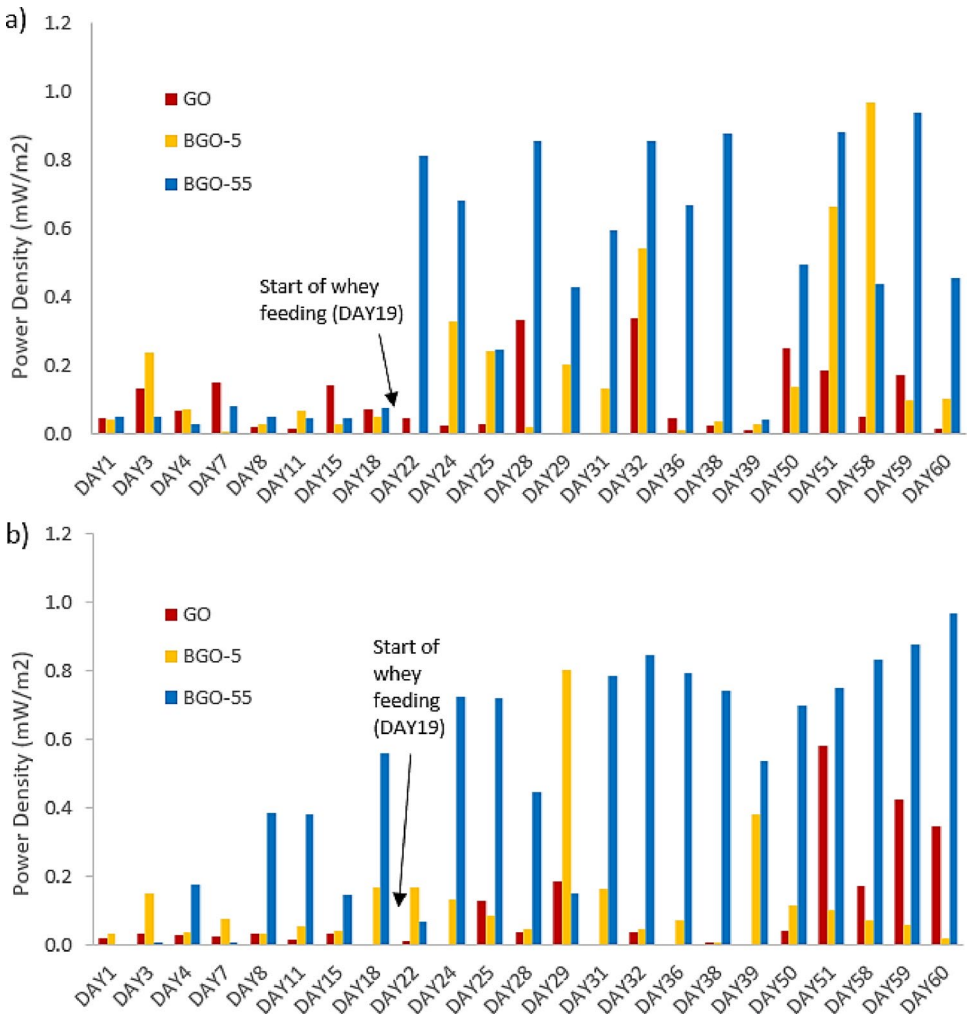


Fig. 11 Variations in power density of PMFC systems with different (a) anode electrode+catalyst-loaded PMFCs, (b) cathode electrode+catalyst-loaded PMFCs (50 kΩ external resistance)

interaction within the oxygen-rich graphene oxide framework. Previous literature reports have also demonstrated that ultrasonication-assisted treatment of defect-rich GO can promote the formation of boron–oxygen–carbon bonding configurations under mild conditions prior to high-temperature annealing [9]. Therefore, while the exact bonding configuration was definitively confirmed, the combined compositional, structural, and electrochemical evidence suggests that boron incorporation in BGO-55 is associated with defect sites rather than arising purely from physical adsorption. These findings are consistent with the hypothesis that boron-associated defect sites enhance catalytic activity by promoting more favorable ORR pathways and accelerating interfacial electron transfer. Moreover, pronounced power increase shown in Fig. 11 for BGO-55-loaded systems after whey addition suggests a synergistic interaction between catalyst structure and substrate availability. While whey supplementation stimulated microbial metabolism and electron production at the anode, the defect-enriched and boron-modified graphene oxide cathode also enabled more efficient electron harvesting and oxygen reduction. This cooperative effect enhanced bio-anodic activity and improved cathodic kinetics ultimately resulted in amplified bioelectrochemical performance. To summarize the discussions above and to clearly illustrate the superior performance of BGO-55 compared to the other electrocatalysts tested in this study, a schematic representation highlighting the key indicators from synthesis and characterization to performance evaluation was presented in Fig. 12.

4 Conclusion

This study demonstrates that low-temperature ultrasonication-assisted boron incorporation into electrochemically exfoliated graphene oxide significantly enhances PMFC performance. When applied in PMFC systems, BGO-55 achieved markedly improved power output compared to GO in both anode- and cathode-modified configurations. Among the tested materials, BGO-55 exhibited the highest

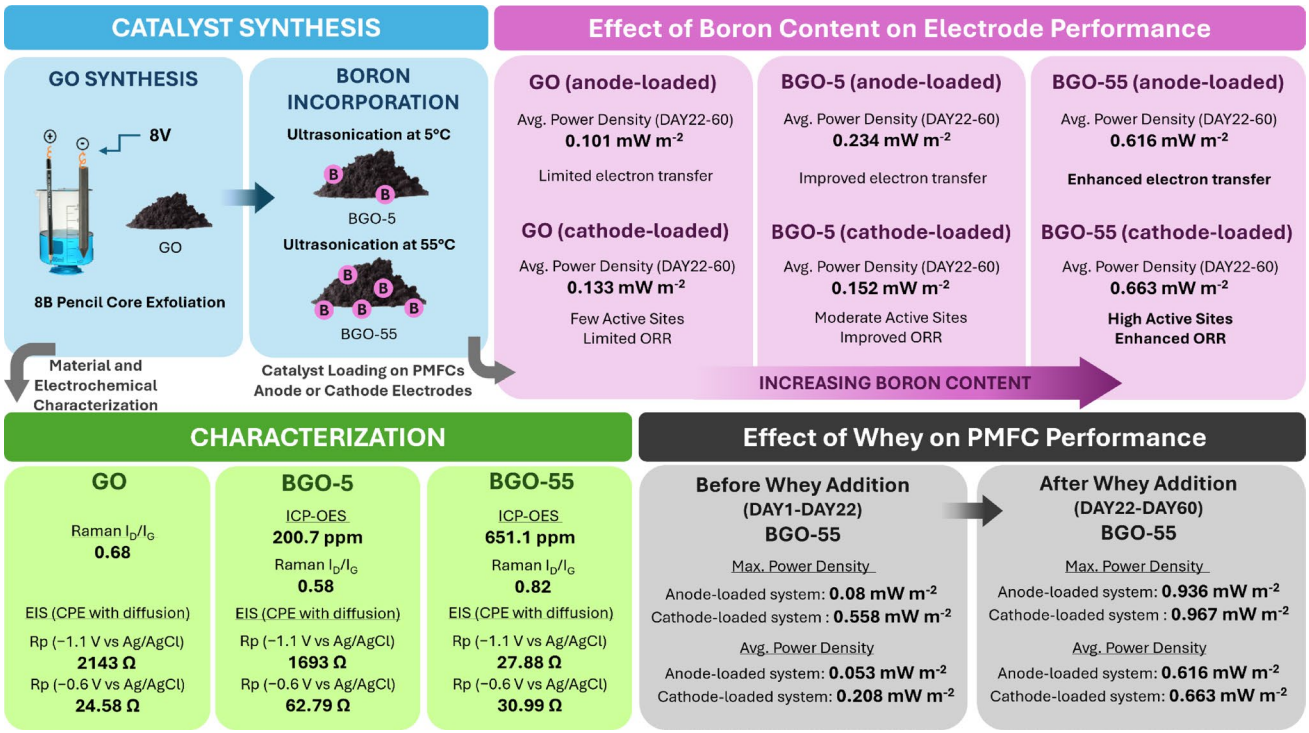


Fig. 12 Comprehensive schematic illustration of graphene oxide (GO) synthesis via electrochemical exfoliation, ultrasonication-assisted boron incorporation (BGO-5 and BGO-55), their electrochemical characterization (Raman, ICP-OES, EIS) and the effect of boron content and catalyst loading (anode/cathode) on PMFC performance, as well as the enhancement observed after whey addition

overall electrochemical performance under whey feeding conditions. These results confirm that increased boron content and defect density contribute to improved electron harvesting at the anode and enhanced oxygen reduction kinetics at the cathode. This improvement is attributed to the formation of defect-rich and electron-deficient active sites, which promote oxygen adsorption and accelerate charge transfer, as supported by Raman, ICP-OES, and EIS analyses. Moreover, cheese whey supplementation significantly boosted bioelectrochemical activity across all configurations, demonstrating a synergistic interaction between catalyst structure and substrate availability. This combined effect highlights the critical role of both catalyst design and substrate enrichment in improving PMFC efficiency. The combined strategy of scalable graphene oxide production, mild-temperature boron incorporation, and agro-industrial waste utilization provides a practical pathway toward improved PMFC efficiency and sustainable renewable energy generation.

Acknowledgements The authors gratefully acknowledge the support of the Middle East Technical University Central Laboratory, where Raman spectroscopy were carried out, and TENMAK Boron Research Institute for performing the ICP-OES measurements. The authors also thank the technical staff of both institutions for their assistance during the characterization studies.

Funding Open access funding provided by the Scientific and Technological Research Council of Türkiye (TÜBİTAK).

Declarations

Conflict of interest The authors declare that they have no known competing financial interests or personal relationships that could have appeared to influence the work reported in this paper.

Open Access This article is licensed under a Creative Commons Attribution 4.0 International License, which permits use, sharing, adaptation, distribution and reproduction in any medium or format, as long as you give appropriate credit to the original author(s) and the source, provide a link to the Creative Commons licence, and indicate if changes were made. The images or other third party material in this article are included in the article's Creative Commons licence, unless indicated otherwise in a credit line to the material. If material is not included in the article's Creative Commons licence and your intended use is not permitted by statutory regulation or exceeds the permitted use, you will need to obtain permission directly from the copyright holder. To view a copy of this licence, visit http://creativecommons.org/licenses/by/4.0/.

References

1. Kuleshova T, Rao A, Bhadra S et al (2022) Plant microbial fuel cells as innovative agro-technology for green energy. Biomass Bioenergy 167:106629
2. Martinez RDR (2024) Plant–microbial fuel cell for electrical generation through living plants: internal resistance insight. Clean Energy 8(5):45–53

3. Gürbüz T, Günay ME, Tapan NA (2024) Machine learning solutions for enhanced performance in plant-based microbial fuel cells. Int J Hydrogen Energy 78:1060–1069
4. Helder M, Strik DPBTB, Hamelers HVM, Buisman CJN (2012) The flat-plate plant-microbial fuel cell: effect of a new design on internal resistances. Biotechnol Biofuels 5:70
5. Pandit S, Das D (2018) Principles of microbial fuel cells for power generation. Microbial Fuel Cell
6. Goto Y, Yoshida N, Umeyama Y, Yamada T, Tero R, Hiraishi A (2015) Enhancement of electricity production by graphene oxide in soil microbial fuel cells and plant microbial fuel cells. Front Bioeng Biotechnol 3:42. https://doi.org/10.3389/fbioe.2015.00042
7. Deng H, Chen Z, Zhao F (2012) Energy from plants and microorganisms: Progress in plant–microbial fuel cells. Chemsuschem 5(6):1006–1011. https://doi.org/10.1002/cssc.201100257
8. Banerjee A, Calay RK, Mustafa M (2022) Review on material and design of anode for microbial fuel cell. Energies 15:2283
9. Zhang M, Tao H, Liu Y et al (2019) N and B codoped graphene oxide for ORR. ACS Sustainable Chem Eng 7:3434–3442
10. Wang L, Sofer Z, Šimek P, Tomandl I, Pumera M (2013) Boron-doped graphene: scalable and tunable p-type carrier concentration doping. J Phys Chem C 117:23251–23257. https://doi.org/10.1021/jp405169j21
11. Xu X, Yuan T, Zhou Y, Li Y, Lu J, Tian X, Wang D, Wang J (2014) Facile synthesis of boron and nitrogen-doped graphene as efficient electrocatalyst for the oxygen reduction reaction in alkaline media. Int J Hydrog Energy 39(29):16043–16052. https://doi.org/10.1016/j.ijhydene.2013.12.079
12. Yan J, Tjandra R, Fang H et al (2018) Boron acid catalyzed synthesis of porous graphene sponge. Diam Relat Mater 89:114–121
13. Seenukool N, Phannakham P, Srimueng N et al (2023) Graphene oxide synthesis via electrochemical exfoliation of pencil core. Materials Today: Proceedings
14. Tafoya JPV, Doszczeczko S, Titirici MM, Sobrido ABJ (2022) Enhancement of the electrocatalytic activity for the oxygen reduction reaction of boron-doped reduced graphene oxide via ultrasonic treatment. Int J Hydrogen Energy 47:5462–5473
15. Parvez K, Wu ZS, Li R et al (2014) Exfoliation of graphite into graphene in inorganic salt solutions. J Am Chem Soc 136:6083–6091
16. Liu J, Poh CK, Zhana D et al (2013) Improved synthesis of graphene flakes via multiple electrochemical exfoliation. Nano Energy 2:377–386
17. Chen K, Xue D, Komarneni S (2017) Nanoclay assisted electrochemical exfoliation of pencil core to high conductive graphene thin-film electrode. J Colloid Interface Sci 487:156–161. https://doi.org/10.1016/j.jcis.2016.10.028
18. Jiwarawat N, Leukulwatanachai T, Subhakornphichan K, Limwathanagura S, Wanotayan S, Atthi N, Pankiew A, Pungetmongkol P (2024) Electrochemical exfoliation of graphene from pencil lead. Sci Rep 14:15892. https://doi.org/10.1038/s41598-024-66825-0
19. Kelly PT, He Z (2014) Understanding the application niche of microbial fuel cells in a cheese wastewater treatment process. Bioresour Technol 157:154–160
20. Makanjuola T, Adegoke A (2019) The effects of whey waste on soil composition and crop yield. Agric Environ Sci 33(4):251–259
21. Tremouli A, Antonopoulou G, Bebelis S, Lyberatos G (2013) Operation of MFC fed with pretreated cheese whey. Bioresour Technol 131:380–389
22. Logan BE, Hamelers B, Rozendal R et al (2006) Microbial fuel cells: methodology and technology. Environ Sci Technol 40:5181–5192
23. Min B, Logan BE (2004) Electricity generation from swine wastewater using MFCs. Water Res 38(20):4947–4956
24. Liu H, Ramnarayanan R, Logan BE (2004) Production of electricity during wastewater treatment in a single chamber MFC. Environ Sci Technol 38:2281–2285
25. Kumar R, Singh L, Wahid ZA (2016) Role of microbial fuel cells in wastewater treatment and energy production. Environ Technol Innov 4:150–162
26. Gómez X, Cuetos MJ, Prieto JI, Morán A, García AI (2017) Valorization of livestock waste and cheese whey for electricity production in a microbial fuel cell. Waste Biomass Valorization 8:2351–2360
27. Song T, Zhang X, Angelidaki I (2021) Effect of cathodic culture on wastewater treatment and power generation. Bioresour Technol 333:125198
28. Watson KS (1978) Continuing impact of the environmental era on dairy industry. Whey Products Conference, Minneapolis, 30–52
29. Draycott AP (2006) Sugar Beet. Wiley, Oxford. https://doi.org/10.1002/9780470751114
30. Oladipo AA, Ahmad M (2025) Energy-efficient ion recovery from water using electro-driven membranes: a comprehensive critical review. Water 17(16):2456
31. Ibrahim AA, Oladipo AA, Gazi M (2025) Electrochemical-based and hybrid technologies: remediation strategies and resource recovery from dairy wastewater. ACS ES&T Water 5(5):2041–2069
32. Sousa MC, Buchanan JW (2000) Observational models of graphite pencil materials. Comput Graph Forum 19(1):27–49
33. Htwe YZN, Mariatti M, Chin SY (2020) Fabrication of graphene by electrochemical intercalation method and performance of graphene/PVA composites as stretchable strain sensor. Arab J Sci Eng. https://doi.org/10.1007/s13369-020-04807-w
34. Liu J, Yang H, Zhen SG, Poh CK, Chaurasia A, Luo J, Wu X, Yeow EKL, Sahoo NG, Lin J, Shen Z (2013) A green approach to the synthesis of high-quality graphene oxide flakes via electrochemical exfoliation of pencil core. RSC Adv 3:11745. https://doi.org/10.1039/c3ra41366g
35. Achee TC, Sun W, Hope JT, Quitzau SG, Sweeney CB, Shah SA, Habib T, Green MJ (2018) High-yield scalable graphene nanosheet production from compressed graphite using electrochemical exfoliation. Sci Rep 8:14525. https://doi.org/10.1038/s41598-018-32741-3
36. Gong Y, Ping Y, Li D, Luo C, Ruan X, Fu Q, Pan C (2017) Preparation of high-quality graphene via electrochemical exfoliation and spark plasma sintering and its applications. Appl Surf Sci 397:213–219. https://doi.org/10.1016/j.apsusc.2016.11.153
37. Sevilla M, Ferrero GA, Fuertes AB (2016) Aqueous dispersions of graphene from electrochemically exfoliated graphite. Chem Eur J 22(48):17351–17358. https://doi.org/10.1002/chem.201603321
38. Yılmaz Mertsoy E, Korucu H (2024) Bor bileşiklerinin GO sentezinde kullanılması. Afyon Kocatepe Univ J Sci Eng 24(5):1235–1241
39. Chen K, Xue D (2014) Preparation of colloidal graphene in quantity by electrochemical exfoliation. J Colloid Interface Sci 436:41–46. https://doi.org/10.1016/j.jcis.2014.08.057
40. Ferrari AC (2007) Raman spectroscopy of graphene and graphite: disorder, electron–phonon coupling, doping and nonadiabatic effects. Solid State Commun 143(1):47–57
41. Yazıcı M, Tiyek İ, Ersoy MS et al (2016) Grafen oksit sentezi ve karakterizasyonu. Gazi Univ J Sci 4:41–48
42. Khai TV, Na HG, Kwak DS et al (2012) Structural and optical properties of boron-doped and undoped graphene oxide films. Chem Eng J 211–212:369–377
43. Ferrari AC, Robertson J (2000) Interpretation of Raman spectra of disordered and amorphous carbon. Phys Rev B 61(20):14095
44. Jiang D, Sumpter BG, Dai S (2006) Unique chemical reactivity of a graphene nanoribbon's zigzag edge. J Chem Phys 126:134701

45. Liu H, Liu Y, Zhu D (2011) Chemical doping of graphene. J Mater Chem 21:3335–3345
46. Sheng W (2010) Electrocatalytic activities of supported Pt nanoparticles for low-temperature fuel cell applications(Doctoral dissertation, Massachusetts Institute of Technology)
47. Gateman SM, Gharbi O, De Melo HG, Ngo K, Turmine M, Vivier V (2022) On the use of a constant phase element (CPE) in electrochemistry. Curr Opin Electrochem 36:101133
48. Abouzari MS, Berkemeier F, Schmitz G, Wilmer D (2009) On the physical interpretation of constant phase elements. Solid State Ionics 180(14–16):922–927
49. Hirschorn B, Orazem ME, Tribollet B, Vivier V, Frateur I, Musiani M (2010) Constant-phase-element behavior caused by resistivity distributions in films: I. Theory. J Electrochem Soc 157(12):C452
50. Huang J (2018) Diffusion impedance of electroactive materials, electrolytic solutions and porous electrodes: Warburg impedance and beyond. Electrochim Acta 281:170–188
51. Wetser K, Dieleman K, Buisman CJN, Strik DPBTB (2017) Electricity from wetlands: Tubular plant microbial fuels with silicone gas-diffusion biocathodes. Appl Energy 185:642–649. https://doi.org/10.1016/j.apenergy.2016.10.122
52. Azri YM, Tou I, Sadi M, Benhabyles L (2018) Bioelectricity generation from three ornamental plants: *Chlorophytum comosum, Chasmanthe floribunda* and *Papyrus diffusus*. Int J Green Energy. https://doi.org/10.1080/15435075.2018.1432487
53. Pamintuan KRS, Sanchez KM (2019) Power generation in a plant-microbial fuel cell assembly with graphite and stainless steel electrodes growing *Vigna radiata*. *IOP Conference Series: Materials Science and Engineering, 703*, 012037. https://doi.org/10.1088/1757-899X/703/1/012037
54. Sudirjo E, Buisman CJN, Strik DPBTB (2019) Activated carbon mixed with marine sediment is suitable as bioanode material for *Spartina anglica* sediment/plant microbial fuel cell: Plant growth, electricity generation, and spatial microbial community diversity. Water 11(9):1810. https://doi.org/10.3390/w11091810
55. Guan C-Y, Yu C-P (2020) Evaluation of plant microbial fuel cells for urban green roofs in a subtropical metropolis. Sci Total Environ. https://doi.org/10.1016/j.scitotenv.2020.142786. Advance online publication
56. Tongphanpharn N, Guan C-Y, Chen W-S, Chang C-C, Yu C-P (2023) Evaluation of long-term performance of plant microbial fuel cells using agricultural plants under the controlled environment. Clean Technol Environ Policy 25:633–644. https://doi.org/10.1007/s10098-021-02222-9
57. Timmers RA, Strik DPBTB, Hamelers HVM, Buisman CJN (2010) Long-term performance of a plant microbial fuel cell with Spar tina anglica. Appl Microbiol Biotechnol 86:973–981

Publisher's Note Springer Nature remains neutral with regard to jurisdictional claims in published maps and institutional affiliations.